

WIND TUNNEL ANALYSIS OF A SPACE RE-ENTRY VEHICLE AT LOW-SPEED CONDITIONS

Nicolina Montella^{1,2}, Gareth A. Vio³, Luigi Iuspa¹, Andrea Aprovitola¹, Giuseppe Pezzella¹, & Antonio Viviani¹

¹ Università della Campania "Luigi Vanvitelli", Dipartimento di Ingegneria. Aversa. Italy.
²CIRA, The Italian Aerospace Research Centre, Capua. Italy.
³School of Aerospace, Mechanical and Mechatronic Engineering. The University of Sydney, Sydney. Australia.

Abstract

This paper deals with low-speed wind tunnel analysis of six different aeroshapes developed within a research activity devoted to the design of a crew return vehicle from servicing low Earth orbit. Aerodynamic configurations are obtained by means of well-established multi-disciplinary optimization methodologies aimed to find out the best architecture and shape for the re-entry vehicle. A proprietary skeleton-based integral soft object methodology has been exploited to parametrically build different vehicle shapes starting from a consolidated lifting body geometry coming from previous studies. Vehicle configurations are mainly characterized by different vertical surfaces (*i.e.*, vertical tail vs V-tail), extended winglets and blended canopy. Aeroshapes under investigation are obtained as a combination of vertical/v-tail surfaces and/or winglets. Finally, to characterize the low-speed aerodynamic behaviour compatible with landing conditions, several wind tunnel test campaigns have been carried out, and results described in detail.

Keywords: Crew Return Vehicle, LEO support services, Multi-Disciplinary Optimization, Low-speed wind tunnel analysis, Skeleton-based integral soft objects.

1. Introduction

The increased demands and proposals for suborbital space activities experienced in recent years are boosting design and development of fully reusable re-entry vehicles from Low Earth Orbit (LEO) with a high level of reliability, sustainability, and low operating costs. Current Crew Return Vehicles (CRVs) are essentially designed to support the International Space Station (ISS) during service operations as an alternative to traditional capsule-based systems operating on low-lifting trajectories. Re-entry vehicles currently under study are expected to exhibit superior control and comfort qualities compared to capsules (i.e., low q-loads on the order of magnitude of unity) and allow a safe landing on conventional runways. Specifically, these qualities are also very attractive and desirable for suborbital space tourism, because of the limited physiological stress which can be withstood by civilian crews without specific training. In this framework, this article considers well-established Multidisciplinary Optimization (MDO) methodologies to define the optimal architecture of a CRV by identifying a set of optimal configurations. In particular, the proprietary SBISO (Skeleton-based Integral Soft Object) methodology [1] is proposed to detail the morphology of a pre-existing lifting body (see Fig. 1), coming from previous studies [2], by adding a canopy and vertical surfaces (vertical tail or V-tail) and/or winglets to characterize the static lateral-directional stability of the vehicle [3]. A multi-disciplinary design optimization procedure was developed, and six aeroshapes were

A multi-disciplinary design optimization procedure was developed, and six aeroshapes were identified by opportunely combining vertical surfaces and winglets.

Finally, to better characterize the low-speed aerodynamics of these configurations, an extended test campaign was performed in the 4x3 ft subsonic Wind Tunnel (WT) facility at the School of Aeronautical Engineering of the University of Sydney [4].

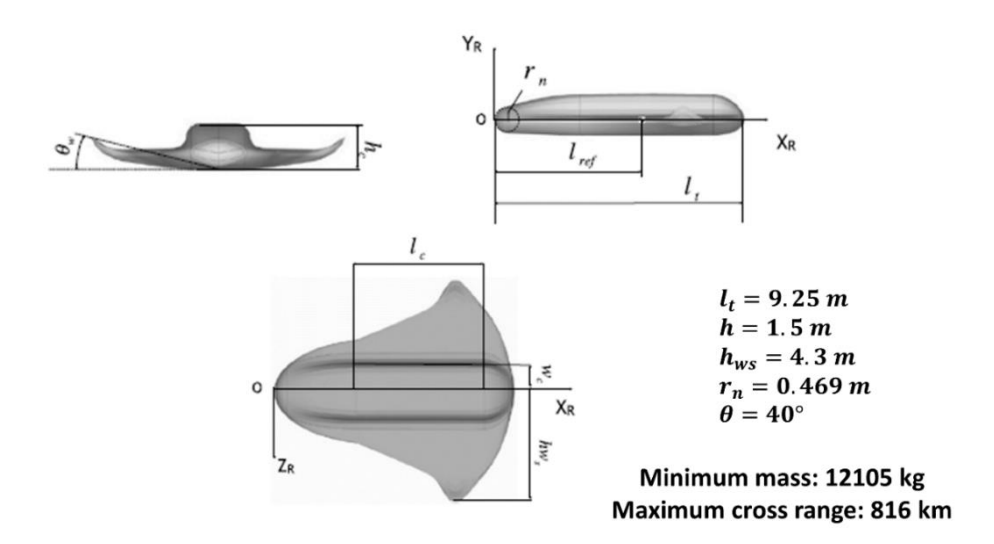


Fig. 1 – Pre-existent, optimized aeroshape of the CRV.

The aim of this experimental investigation is to address the understanding of how aerodynamic force and moment coefficients of aeroshapes at 30 m/s, *i.e.*, landing conditions, through a range of different angles of attack and sideslip. Recall that, assessing landing condition aerodynamics is of paramount importance for such hypersonically optimized low aspect ratio wing aeroshapes [5] [6]. Aeroshape test beds are obtained by means of 3D printing techniques, using an assembly of three-dimensional printed pieces built using a NupBox® 3D printer, available in the FabLab of the University of Sydney [7].

2. The Skeleton-Based Integral Soft Objects Technique

The SBISO technique was originally developed to model structural self-stiffened panels with free topology [1]. The method employs mathematical objects based on a morphological skeleton called primitives and field function irradiated by skeletons that arbitrarily modify a host domain Ω , *i.e.*, a user-defined computational grid able to model the prescribed structure to analyze, see Fig. 2.

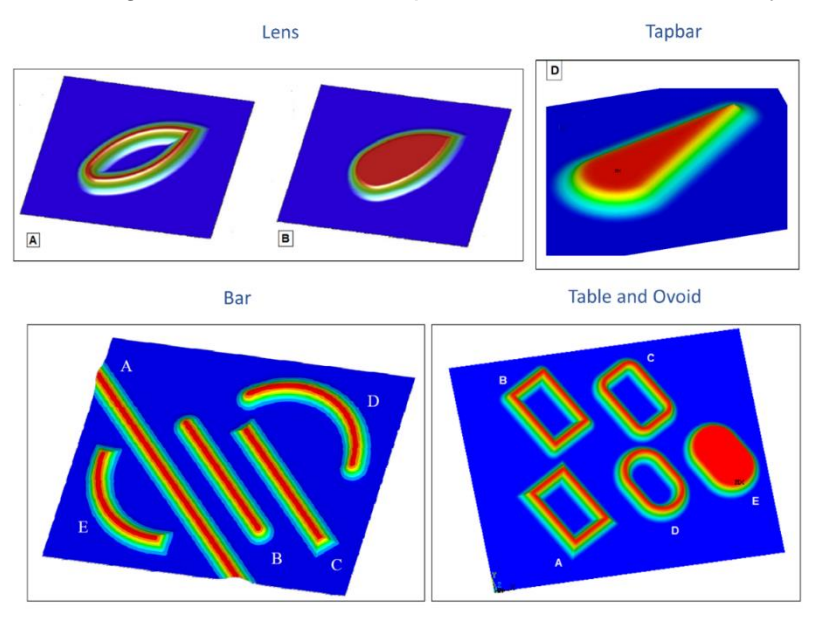


Fig. 2 – A simple plane grid modified by with different SBISO objects.

The main features of this technique are summarized as follows:

✓ SBISO primitives operate at a higher level of abstraction than normal FEM modeling actions. This makes it easy to handle arbitrary computational grids with built-in parametric stiffening

regions;

- ✓ the method does not require or employ any supporting geometry; moreover, the semantic value of the computational grid is ignored by the method;
- ✓ any user-defined mesh can be used as a host domain (flat, single or double curved, open or closed, non-manifold):
- ✓ SBISO primitives freely blend together when overlaid. This feature allows an unprecedented topology to be freely generated for the ledge layout. Several merge styles are available at runtime, each of which allows specific interaction;
- ✓ The method comes with several dozen types of primitives with different shapes and assorted topology, designed primarily for structural purposes; additional primitives can be freely added by advanced users using a general development framework outlined by the method;
- ✓ SBISO primitives can be added, resized, translated, reoriented, or temporarily disabled at runtime without limitations or side effects;
- ✓ the morphological/topological structure of the primitives themselves can be changed at runtime, generating a huge variety of derived forms (polymorphism);
- ✓ the method does not require re-meshing, only fast morphing produced with high-performance Fig.s;
- ✓ the entire methodology (procedures and data structure) is inherently designed to take advantage of a massively parallel architecture such as the GPGPU (General-Purpose computing on Graphics Processing Unit).

All the SBISO agents are managed in SSPaM (Self-Stiffened Panel Modeller), a proprietary environment characterized by a user-friendly and robust scripting language. This dedicated environment is incapsulated in the Ansys® Mechanical APDL and can be exploited to perform parametric procedures (i.e., structural optimization, sensitivity analysis, DoE, surface response, etc.) with no side-effects. In the present context, the SBISO technique can be used to produce the entire body of a space vehicle starting from a simple flat parametric mesh just describing the plan form, and special inflation operators that add shape and volume, as illustrated in [3].

3. Winglets and tail modelling

The SBISO technique was applied to add parametric aerodynamic surfaces to the aeroshape represented in Fig. 1. Fig. 3 shows very different aeroshapes and dimensions of the vertical tail by using just one type of parametrically controlled SBISO primitive, namely *Tapbar*.

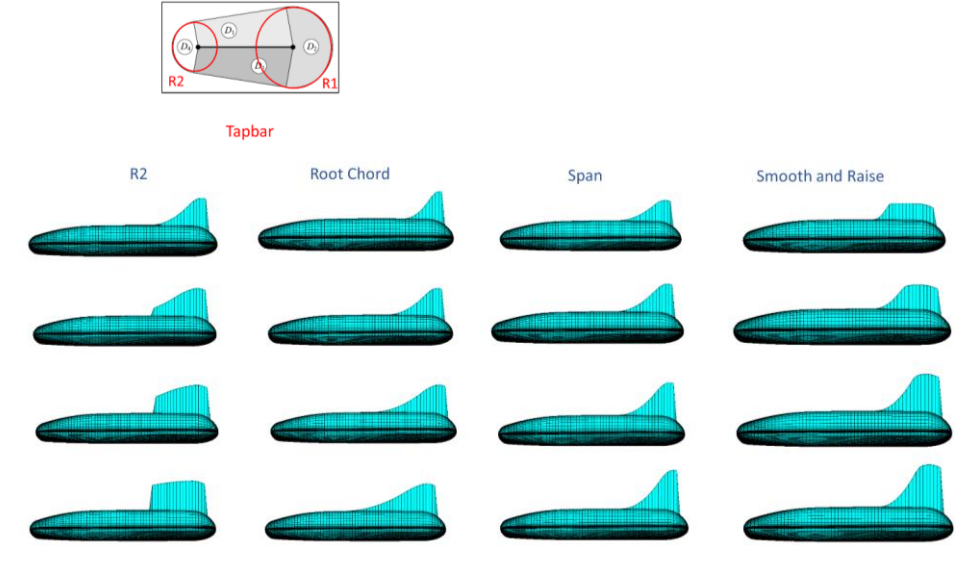


Fig. 3 – Parametrical instances of a vertical tail by a simple *Tapbar* SBISO primitive (no sweep angle).

The SBISO primitive *Tapbar* is a tapered bar that may change its morphological parameters and strength to alter the spatial position of mesh nodes. *Smooth*, *Raise* and *Cut-off* operators can be subsequently applied to refine properly the shape of the tail.

The same trivial approach was used to model a V-tail, simply adding a further *Tapbar* primitive and using the *Vector* operator to introduce both sweep and dihedral angles, see Fig. 4.

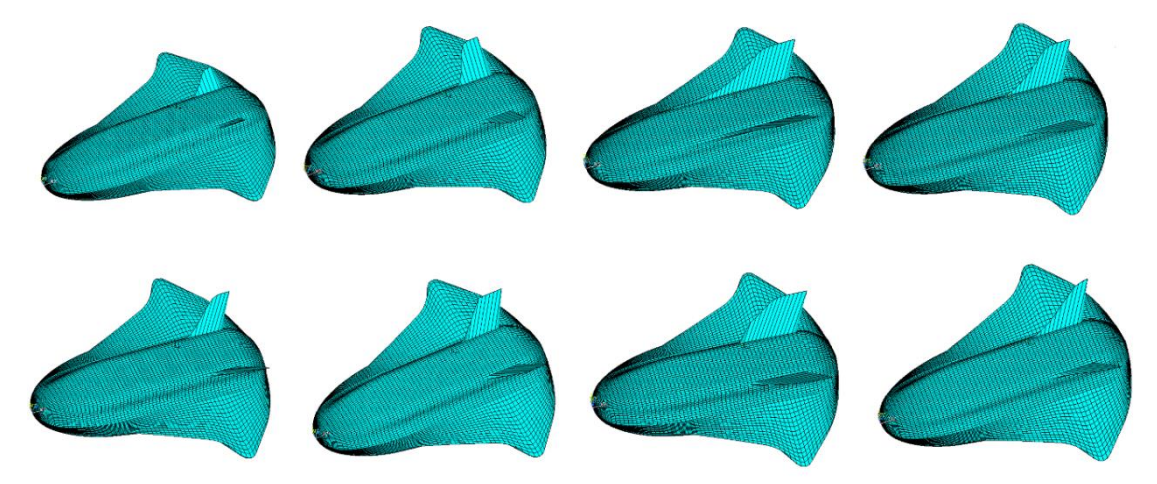


Fig. 4 - V-tail modelling by using a Tapbar SBISO primitive.

The SBISO primitive used to model winglets is a simple infinite-length bar parametrically placed on the vehicle planform, driven by a linear field function, see Fig. 5. This bar can parametrically change its influence radius and strength, generating wing tips with adjustable extension and dihedral angle.

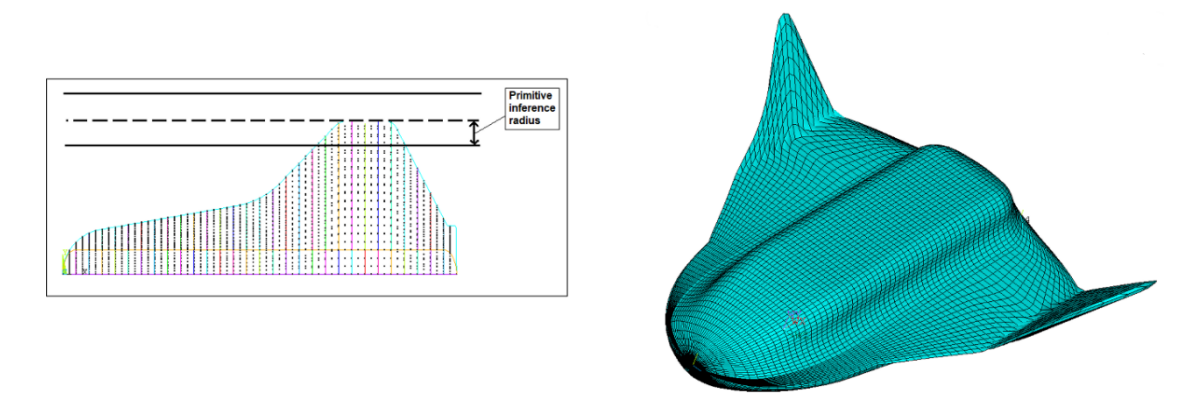


Fig. 5 - Winglets parametric modelling by using an infinite-length bar.

The SBISO method was used also to generate a canopy integrating a rear fairing, see Fig. 6, on the upper front part of the fuselage. A simple combination (blending) of two primitives was used: an *Elliptical Dome* for the canopy and a *Tapbar* for the rear fairing.

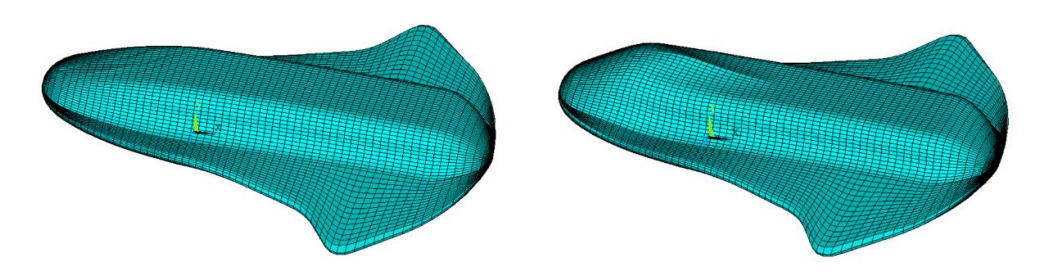


Fig. 6 - Canopy and rear fairing modelling using an Elliptical Dome and a Tapbar SBISO primitive.

4. Multi-disciplinary optimization

The SBISO technique was exploited within an optimization procedure to find out the best shape arrangement of vertical tail, V-tail, winglets and canopy that minimizes the mass satisfying, at the same time, main functional constraints (*i.e.*, heatshield allowable temperature, structural load factor, max touch-down speed, lateral-directional derivatives, and cross-range). The flowchart of the optimization cycle is provided in Fig. 7. For more details see Ref. [8].

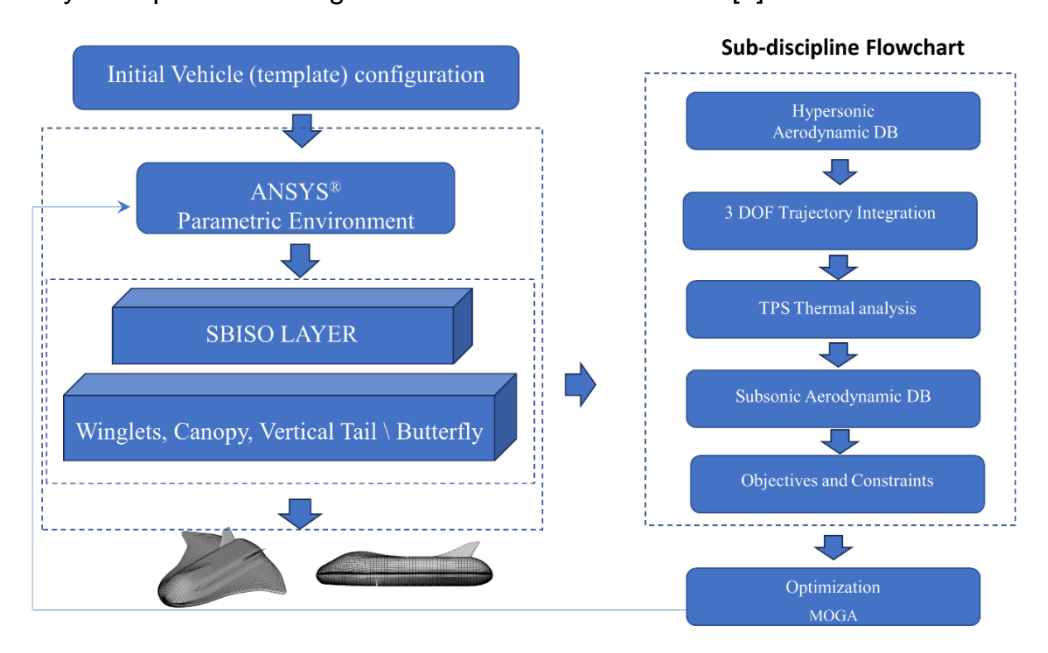


Fig. 7 - Optimization cycle flowchart.

Design variables are defined as follows:

- AW: infinite-length bar half-size in half wingspan percentage (*i.e.*, winglet aspect-ratio), (Fig. 5):
- HW: strength of the infinite-length bar applied to the winglets (Fig. 5) expressed in cabin height percentage;
- XVT: Tapbar centroid position in vehicle chord percentage for the vertical-tail modelling;
- LT: distance between *Tapbar* centers in vehicle chord percentage for the vertical tail and V-tail modelling (*i.e.*, tail root chord length), (Fig. 3);
- RT: *Tapbar* minor circumference radius expressed in cabin half width percentage for vertical tail and V-tail modelling (Fig. 3);
- HT: Tapbar strength in cabin height percentage for the vertical-tail and the V-tail modelling (i.e., tail aspect ratio);
- ST: tail smooth and raise parameter in HT percentage. These operators can raise the *Tapbar* and then cut it smoothly in order to change the shape of the tail in a controlled manner;
- Λ: tail sweep angle;
- Γ: tail dihedral angle;
- μ_{a_0} : initial bank-angle.

The optimization procedure considers the following aero-thermodynamics constraints, structural constraints, and cross-range constraints for all the configurations:

- T_{IN}: internal temperature (≤ 422 K);
- T_{OUT}: external temperature (≤ 2030 K for Reinforced Carbon-Carbon (RCC), ≤ 1760 K for LI-900);
- V_{TD} : touch-down speed (\leq 115 m/s);
- N_{LIM}: load factor (≤ 2.5);

- Q_{LIM} : dynamic pressure (\leq 14 kPa)
- Δ_{ν_n} : cross-range (≥ 500 km).

Constraints for lateral-directional stability are:

- C_{m_n}: longitudinal static stability (≤ 0);
- C_{l_s}: lateral static stability (≤ 0);
- $C_{n_{\theta}}$: directional static stability (≥ 0);
- C^{*}_{ng}: directional static stability (≥ 0).

The aerodynamic performance of these configurations within the optimization process (see Fig. 7) are addressed by means of panel methods, namely APAME and HySIM [9]. APAME is a public domain panel method, based on the potential flow theory, performed to assess aeroshape aerodynamics at subsonic regime [9]. HySIM is an in-house developed code which analyzes vehicle aerodynamics at hypersonic speeds [10]. Details about HySIM tool are provided in 4.1.

4.1 HySIM code implementation for the hypersonic aerodynamic analysis

HySIM stands for Hypersonic Surface Inclination Methods. This tool exploits Newtonian surface inclination methods to address aeroshape hypersonic aerodynamics [11]. The code, based on a fast Ansys® APDL vectorial procedure, can analyze a wide variety of arbitrarily shaped bodies as it supports both structured and unstructured meshes. HySIM implements several methods: Newtonian, Modified Newtonian, Tangent-Cone, Tangent-Wedge, and Modified Newtonian + Prandtl-Meyer.

The user can subdivide the mesh into clusters of elements/panels, and choose the most suitable method for each group. If the user selects one of the first four methods defined in the previous paragraph, the procedure will apply the chosen method to the windward zone, also automatically adding the Prandtl-Meyer expansion to the leeward part.

Conversely, if the user chooses the last method (Modified Newtonian + Prandtl Meyer), Modified Newtonian formulation will be used along with the body until a self-detected location is reached where both pressure and pressure gradients match those that would be calculated from a Prandtl-Meyer expansion.

The accuracy of HySIM in addressing vehicle aerodynamics can be appreciated in Fig. 8, where its predictions for $M_{\infty}=23^{\circ}$ and $\alpha=40^{\circ}$ are compared with results of more reliable hi-fidelity CFD simulations.

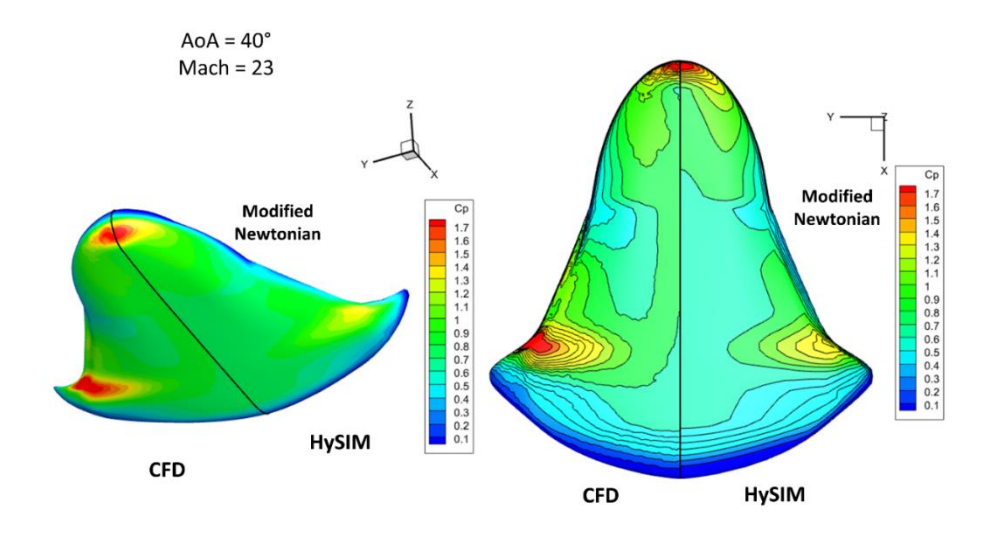


Fig. 8 - CFD and HySIM comparison; pressure field.

4.2 Optimization results

Multidisciplinary optimization provided the six aeroshape candidates summarized from Fig. 9 to Fig. 14, namely aeroshape NM0 (Fig. 9), NM1 (Fig. 10), NM2 (Fig. 11), NM3 (Fig. 12), NM4 (Fig. 13), and NM5 (Fig. 14). The aeroshape NM0 (Fig. 9) is the baseline aeroshape. Analysis of this aeroshape is useful to understand how vertical surfaces (i.e., vertical tail vs V-tail) and/or winglets change aerodynamic characteristics with respect to the baseline configuration. The aeroshape NM1 (Fig. 10) features a little vertical tail and no winglets; it is the result of a minimum mass and maximum cross range multi-objective optimization in which the optimization algorithm is free of varying the dimension and position of the vertical fin in order to satisfy the lateral-directional static stability constraints. The aeroshape NM2 (Fig. 11) shows a V-tail with a dihedral angle of about 48° and no winglets; as the aeroshape NM1, also the aeroshape NM2 is the result of a minimum mass and maximum crossrange multi-objective optimization, but in this case the optimization algorithm changes the dihedral angle and the shape of the V-tail in order to satisfy the lateral-directional static stability constraints. The aeroshape NM3 (Fig. 12) is characterized by the same V-tail of the aeroshape NM2 but, in addition, it features little winglets in order to improve the body longitudinal performances. The aeroshape NM4 (Fig. 13) is characterized by the same vertical tail of the aeroshape NM1, but it also features pronounced winglets.

Finally, the aeroshape NM5 (Fig. 14) features two pronounced winglets and no vertical tail.

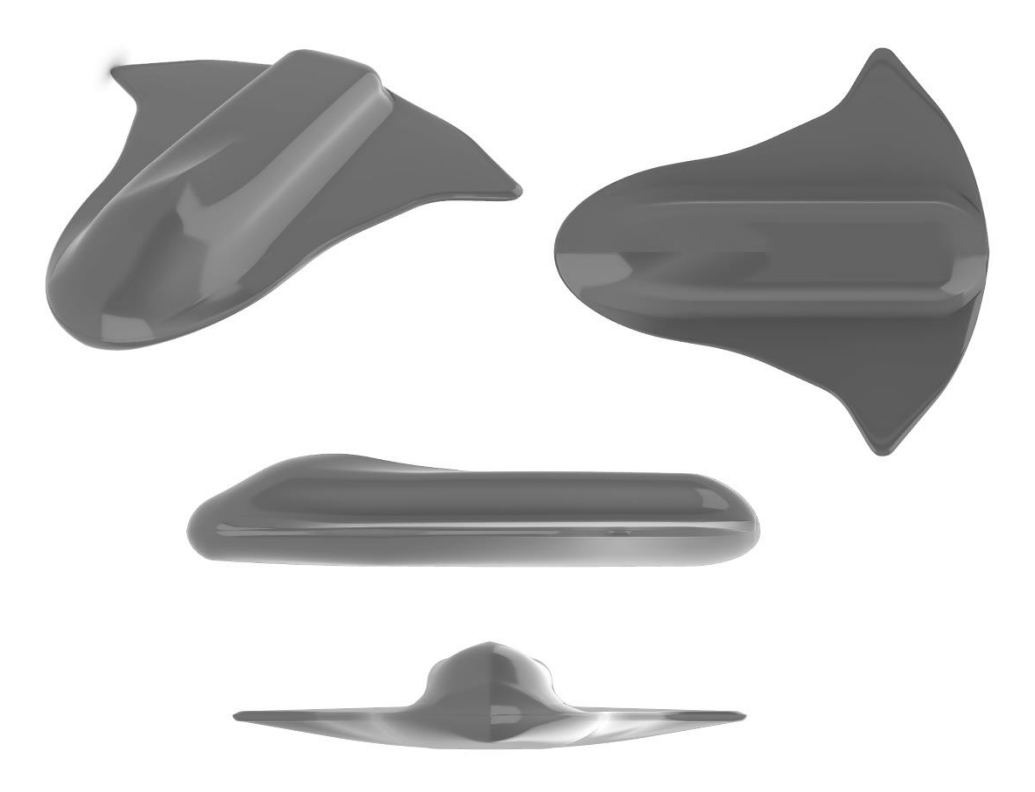


Fig. 9 – Aeroshape NM0.

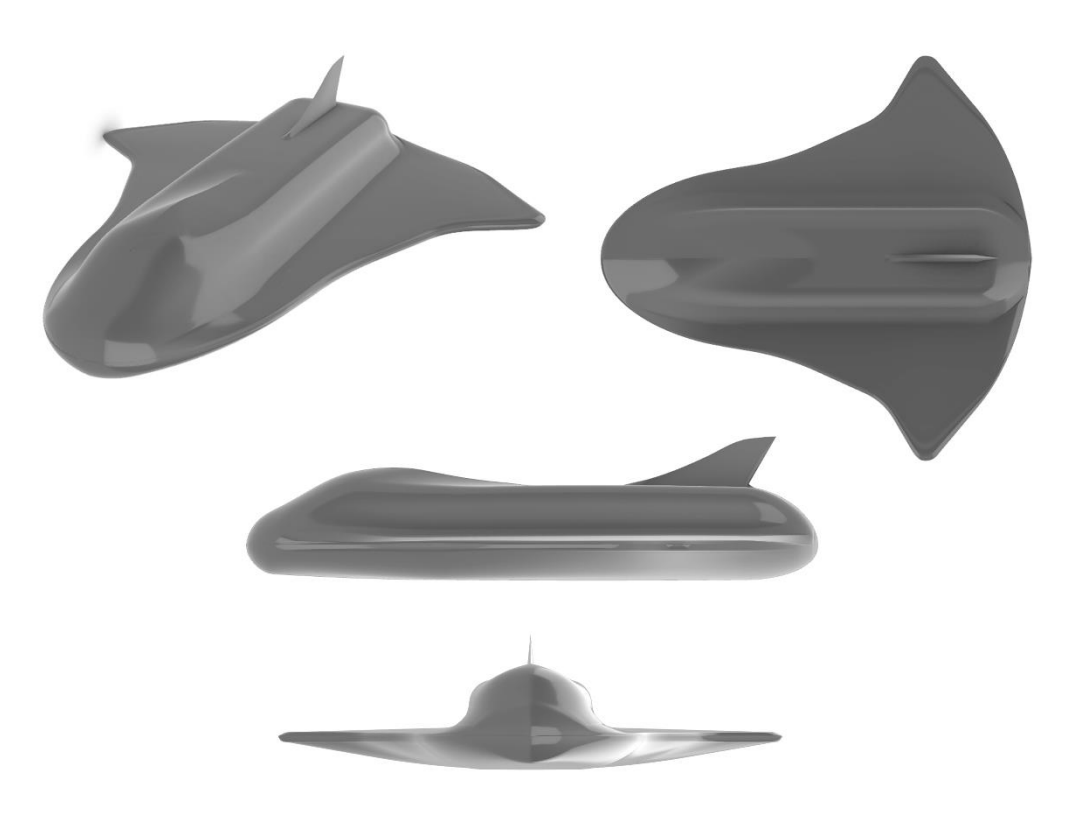


Fig. 10 – Aeroshape NM1.

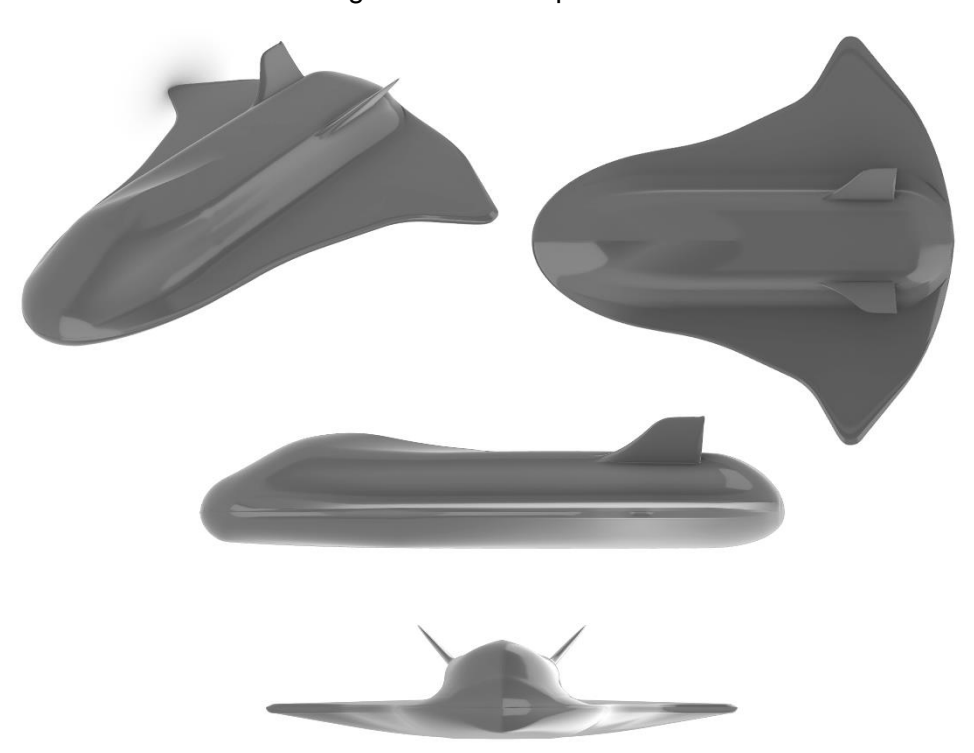


Fig. 11 – Aeroshape NM2.

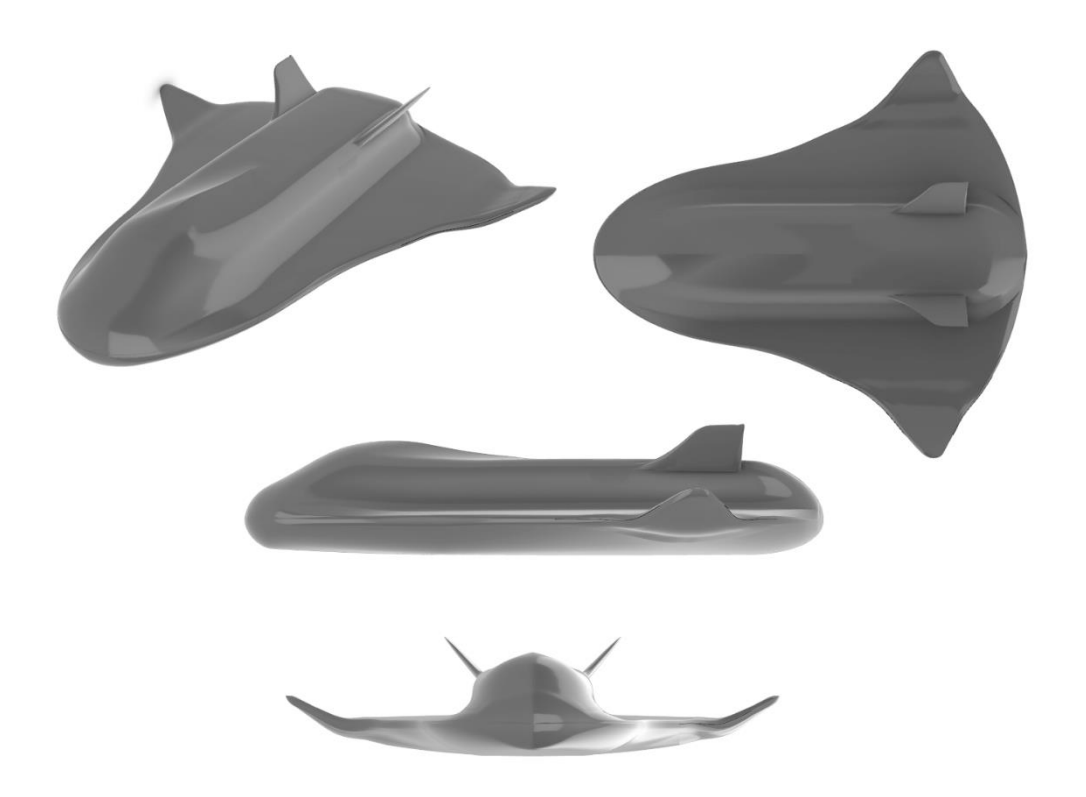


Fig. 12 – Aeroshape NM3.

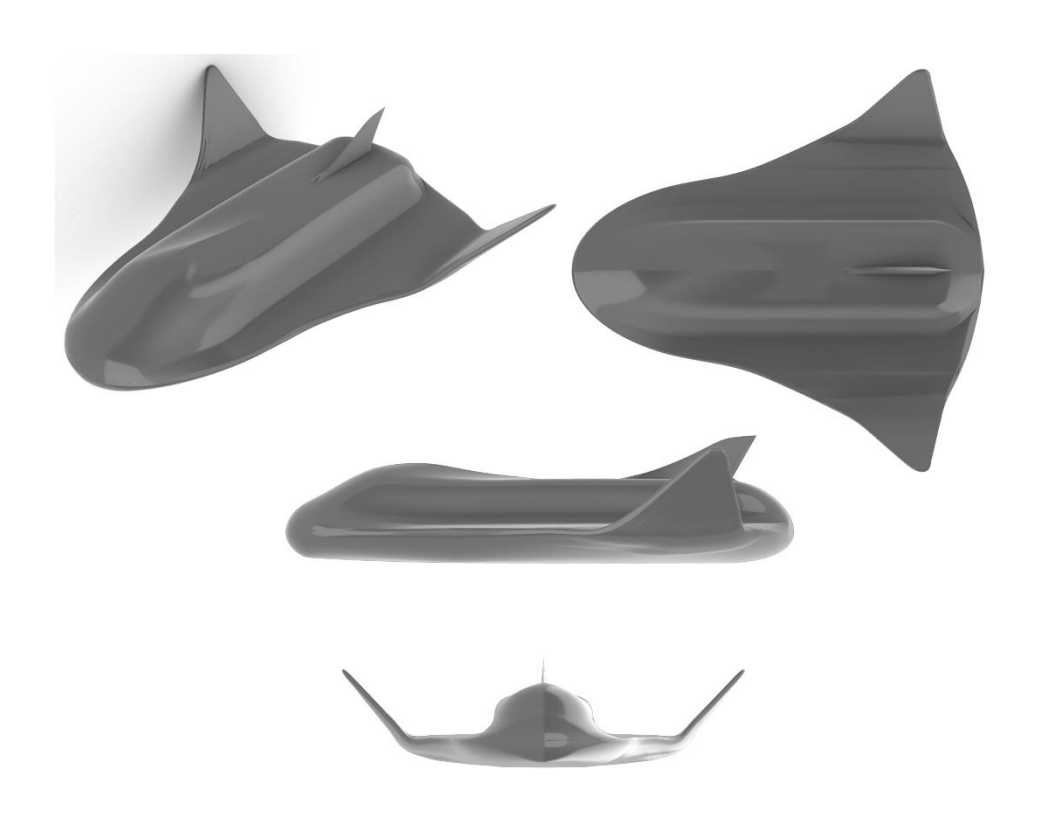


Fig. 13 – Aeroshape NM4.

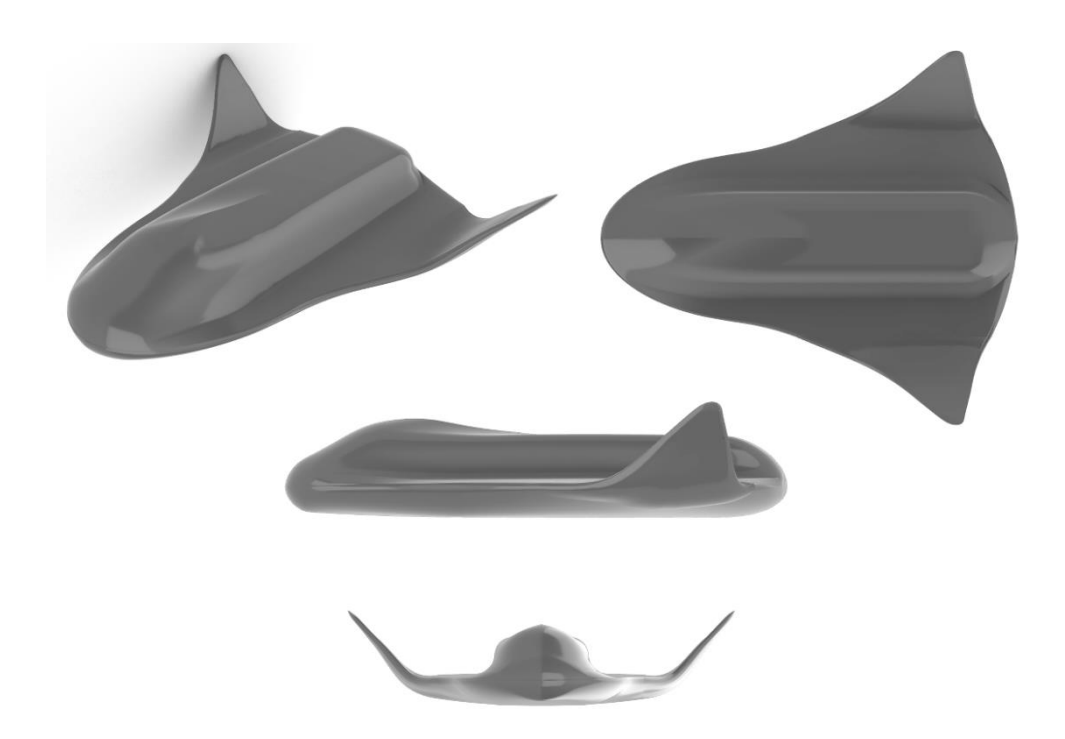


Fig. 14 – Aeroshape NM5.

Table 1 shows the design variables values for all the above configurations.

Table 1 - Design variables.

Aeroshape	AW	HW	XVT	LT	RT	нт	ST	Λ [deg]	Γ [deg]	μ_{a_0} [deg]
NM0	-	-	-	-	-	-	-	-	-	15
NM1	-	-	0.87052	0.20479	0.0063839	0.69131	0.20206	38.380	3.9051	13.001
NM2	-	-	-	0.21193	0.0011619	0.62210	0.44233	13.284	42.270	15.119
NM3	0.21272	0.37175	-	0.25715	0.0012217	0.66838	0.72809	35.893	47.840	13.705
NM4	0.34	1.2	0.87052	0.20479	0.0063839	0.69131	0.20206	38.380	3.9051	13
NM5	0.34	1.2	-	-	-	-	-	-	-	15

Table 2 shows the constraints values for all the above configurations.

Table 2 - Constraints.

Aero- shape	T_{IN}	T _{OUT}	V_{TD}	N _{LIM}	Q_{LIM}	Δ_{y_p} [km]	$C_{m_{lpha}}$	$C_{l_{oldsymbol{eta}}}$	$C_{n_{eta}}$	$\mathcal{C}_{n_{oldsymbol{eta}}}^{*}$
NM0	0	0	1.044	0.44735	0.82586	582.66	-0.12988	-0.018459	-0.0089439	0.0078369
NM1	0	0	1.04815	0.44398	0.83093	519.49	-0.13335	-0.013834	0.00063669	0.013102
NM2	0	0	1.0472	0.44768	0.83058	586.85	-0.029482	-0.0042650	0.012047	0.015710
NM3	0	0	1.0495	0.44483	0.83452	547.26	-0.075605	-0.0049612	0.013879	0.018142
NM4	3313.2	0	1.0912	0.44474	0.89964	528.91	-0.52338	-0.031375	-0.0010394	0.027269
NM5	2964.3	0	1.0871	0.44830	0.89443	593.74	-0.51932	-0.037168	-0.00921	0.024450

Finally, Table 3 shows the objective function value for all the above configurations, i.e., the vehicle mass.

Aeroshape	M_{TOT} [kg]
NM0	12114
NM1	12219
NM2	12352
NM3	12440
NM4	12490
NM5	12386

5. Rapid prototyping with 3D printing techniques

To perform WT tests, a properly scaled body model was built from an assembly of 3D printed parts produced with a NupBox® 3D printer, available in the FabLab of the University of Sydney [5], (see Fig. 15).



Fig. 15 - NupBox FFF/FDM printer.

The NupBox 3D printer is based on Fused Filament Fabrication (FFF) and Fusion Deposit Modelling (FDM) technology. PolyLactic Acid (PLA) filament was used for the 3D printing. In Fig. 16 the required 3D parts are shown, as a result of a proper decomposition to meet the print bed size.



Fig. 16 - 3D printed half central body parts.

To account for all the six aerodynamic configurations, the WT test model is designed and decomposed appropriately so that different wing shapes and vertical tails could be fitted to the same body and combined according to the specific layout of each aeroshape. The model was accurately

assembled/glued first, then sprayed with putty and sanded, repeating the sequence more and more times in order to achieve the smoothest possible surface, see Fig. 17, Fig. 18, and Fig. 19. A final coating of deep-black mat painting was then sprayed.



Fig. 17 – Central body of the model sanded with putty spray.



Fig. 18 - Interchangeable tails refined with putty spray and sanded.



Fig. 19 - Interchangeable wings (aeroshape NM3).

All the six finished configurations painted with a special coating spray are shown from Fig. 20 to Fig. 25.



Fig. 20 - Aeroshape NM0.



Fig. 21 - Aeroshape NM1.



Fig. 22 - Aeroshape NM2.



Fig. 23 - Aeroshape NM3.



Fig. 24 - Aeroshape NM4.



Fig. 25 - Aeroshape NM5.

6. Experimental investigations in WT

Aeroshapes of CRV are typically characterized by configurations with rather blunt leading edges and very low aspect ratios wing to withstand the intense aeroheating expected during re-entry [12]. Although these configurations represent a figure of merit for the CRV at hypersonic speeds, they are penalizing when the vehicle is in the landing phase. Therefore, a subsonic characterization of the aerodynamics is mandatory to verify the capability of performing a safe landing on conventional runway.

With this in mind, several experimental investigations have been performed in the 4x3 ft low-speed WT at the School of Aeronautical Engineering of the University of Sydney. The model, arranged in specific configuration, is mounted in the WT test chamber as shown in Fig. 26.



Fig. 26 – Aeroshape model NM3 installed at University of Sydney's 4x3ft WT.

A special cavity was predisposed in the model to house the load cell (Fig. 29). The model was designed such that the load cell reference base resulted aligned with the center of gravity (CoG) of the model. A moving ballast was provided to adjust the resulting CoG for the different configurations. A removable fit flush fairing was also added to the cavity to assure a smooth flow on the bottom of the model. Testing was performed under constant voltage demand for the tunnel fan, *i.e.*, with an increasing Angle of Attack (AoA), the test section speed was not constant due to blockage effects. The AoA of the model was incremented in discrete steps across a range angle from -5° to 35°. At highest AoA, the degree of blockage approaches 10%, so blockage corrections for the dynamic pressure were considered from Ref. [13]. In particular, Eqs. (1-2) were used:

$$\in_T = \in_{wb} + \in_{sb} = \frac{A_{frontal}}{A_{WT}} \times 0.25 \tag{1}$$

$$q_c = q_a (1 + \epsilon_T)^2 \tag{2}$$

where \in_{wb} is wake blockage and \in_{sb} is solid blockage. A_{WT} is the test section's cross-sectional area, and $A_{frontal}$ is the projected area of the configuration at each AoA condition over the A_{WT} .

The aerodynamic coefficients were calculated using the corrected dynamic pressure computed from Eq. (2). No tip corrections were deemed necessary, due to the short wingspan relative to the test section width. The operative range of the WT is of 10-65 m/s. Assuming a 10% blockage-ratio, a safe factor margin of 10%, and a maximum AoA of 30°, a test bed length of 0.59 m resulted (1/14 scale), with a wingspan of 0.55 m and a reference surface (planform area) of about 0.223 m².

Table 4 - Summary of reference values for the 1:14 scale model.

Parameter	Value		
Reference Area [m ²]	0.223		
Length [m]	0.59		
Span [m]	0.55		
X _{CoG} [m]	0.322		
Y _{CoG} [m]	0		
Z _{CoG} [m]	0.00655		

In Table 4, the main geometric parameters are summarized. These quantities are also considered to provide aerodynamic force and moment coefficients, according to the ISO 1151 standard. The position of the CoG of the test model is measured with respect to a main reference system put at the vehicle nose, with the X-axis along the centerline toward the vehicle aft, and the Z-axis toward the top vehicle. The basic CoG position (related to the NM01 configuration) along the X-axis corresponds to about 55% of the model length (as expected for this category of vehicle). A fine tuning of CoG obtained with a modular and moveable ballast was performed to preliminary cancel any spurious static moments with respect to the load cell reference for each configuration. Aerodynamic data are acquired using an ATI-IA Mini45 6-component load cell attached to an actuated strut on a turntable, allowing both longitudinal and lateral variations in wind direction (see Fig. 26, Fig. 27 and Fig. 28).



Fig. 27 - ATI-IA Mini 45 load cell.



Fig. 28 - 3x4 strut mount.

WT test bed with the load cell fixed inside is depicted in Fig. 29, where the assembly of all 3D printed pieces is also clearly recognizable.

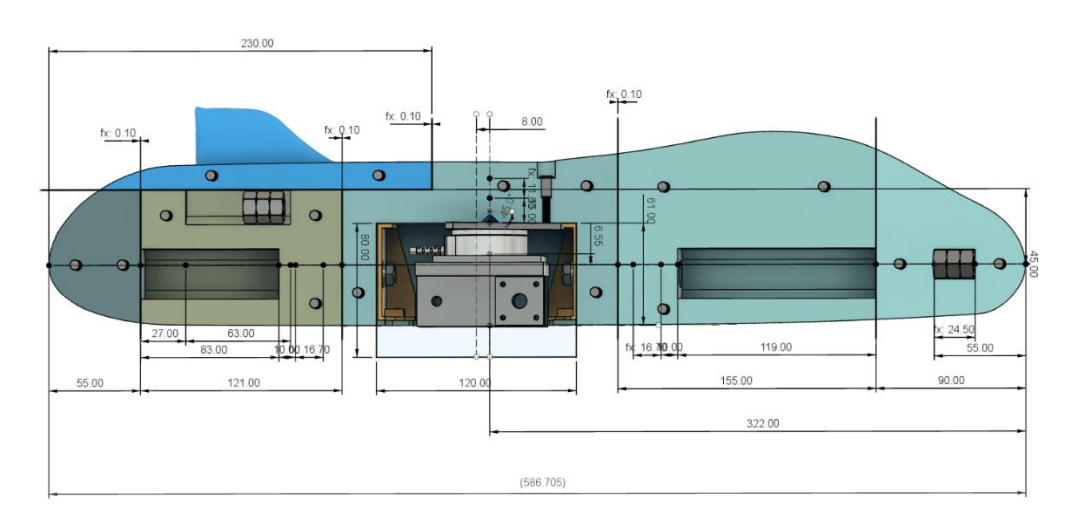


Fig. 29 - Wind tunnel test bed with the load cell.

Finally, in Table 5 the maximum sensing range and the load cell resolution for each axis are reported.

Table 5 - Technical data for the ATI Mini 45 load cell.

	Sensin	g range		Resolution			
Fx, Fy [N]	Fz [N]	Mx, My [Nm]	Mz [Nm]	Fx, Fy [N]	Fz [N]	Mx, My [Nm]	Mz [Nm]
580	1160	20	20	0.25	0.25	0.005	0.0027

Differential pressure measurements are obtained using an MS453DO pressure sensor with the atmospheric pressure provided by a MS5611 barometric pressure sensor. Airspeed measurements are obtained through this data, interfaced via an Arduino Pro Mini to the in-house data acquisition software, yielding an uncertainty value in the velocity measurements of ±0.15 m/s. An accelerometer fixed to the rotating component of the WT mount is used to make AoA measurements, providing an average uncertainty of 0.1° in the measured AoA (and 0.25° maximum error). For further details about the uncertainty calculations and sensor calibrations see [14] and [15]. Discrete changes in the AoA are applied in the pitch-and-pause mode for a given airspeed within the range of interest of [-5°,35°]. The flow is allowed to stabilise for 2 s at each AoA prior to the load cell acquiring data for an additional 2 s at a frequency of 5000 Hz. Comprehensive sensitivity studies were conducted under analogous conditions in this facility which show that this approach is sufficient, see [14] and [15].

7. Results

In the present paper, longitudinal aerodynamic characteristics of the NM0, NM1 and NM2 aeroshapes are discussed in terms of force and moment coefficients. For instance, Fig. 30a-c, Fig. 31a-c, and Fig. 32a-c, provide lift (C_L), drag (C_D), pitching moment (C_M) coefficients, and the lift-to-drag (L/D) of each aeroshape. These aerodynamic coefficients have been acquired during the discrete change in AoA from -5° to 35° at $V_\infty = 30 \, m/s$ ($Re \approx 1.2 \times 10^6$).

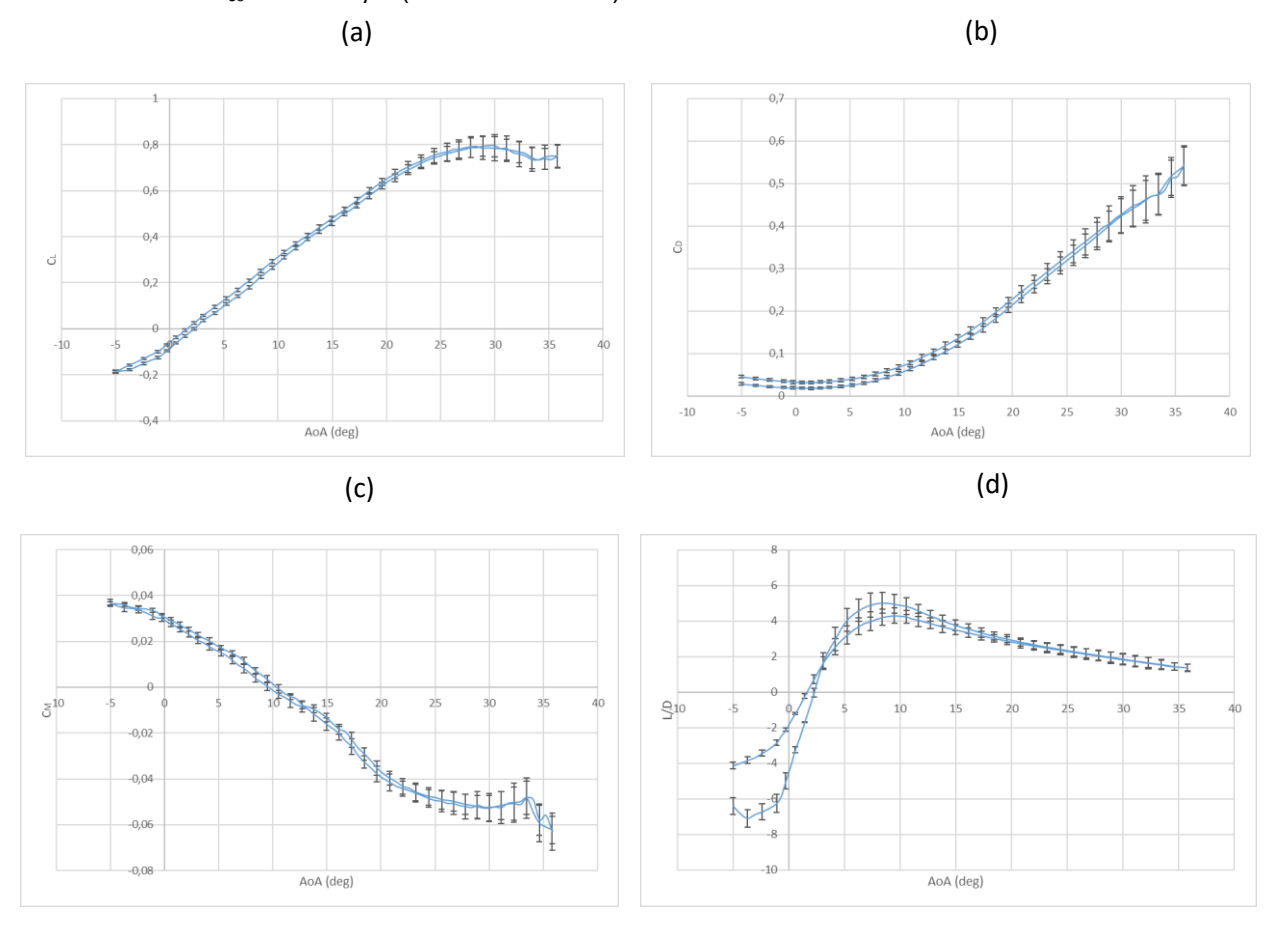


Fig. 30 – NM0 aerodynamics: (a) C_L vs α ; (b) C_D vs α ; (c) C_M vs α (MRP at 0.41% L_{ref}); (d) L/D vs α .

The closeness of the two parts of each curve (Fig. 30, Fig. 31, and Fig. 32) is evidence of the accuracy and repeatability of the measurements. Error bars are given in the form of standard deviations from the mean value, as calculated across 10,000 samples taken at each AoA α for both parts of each curve. Lift and drag coefficients, shown in Fig. 30a-b, Fig. 31a-b, and Fig. 32a-b, exhibit the typical longitudinal characteristics of a slender, delta-wing aircraft. Lift increases monotonically throughout the AoA range, contributing a significant lift-induced component to the drag coefficient at high angles [16].

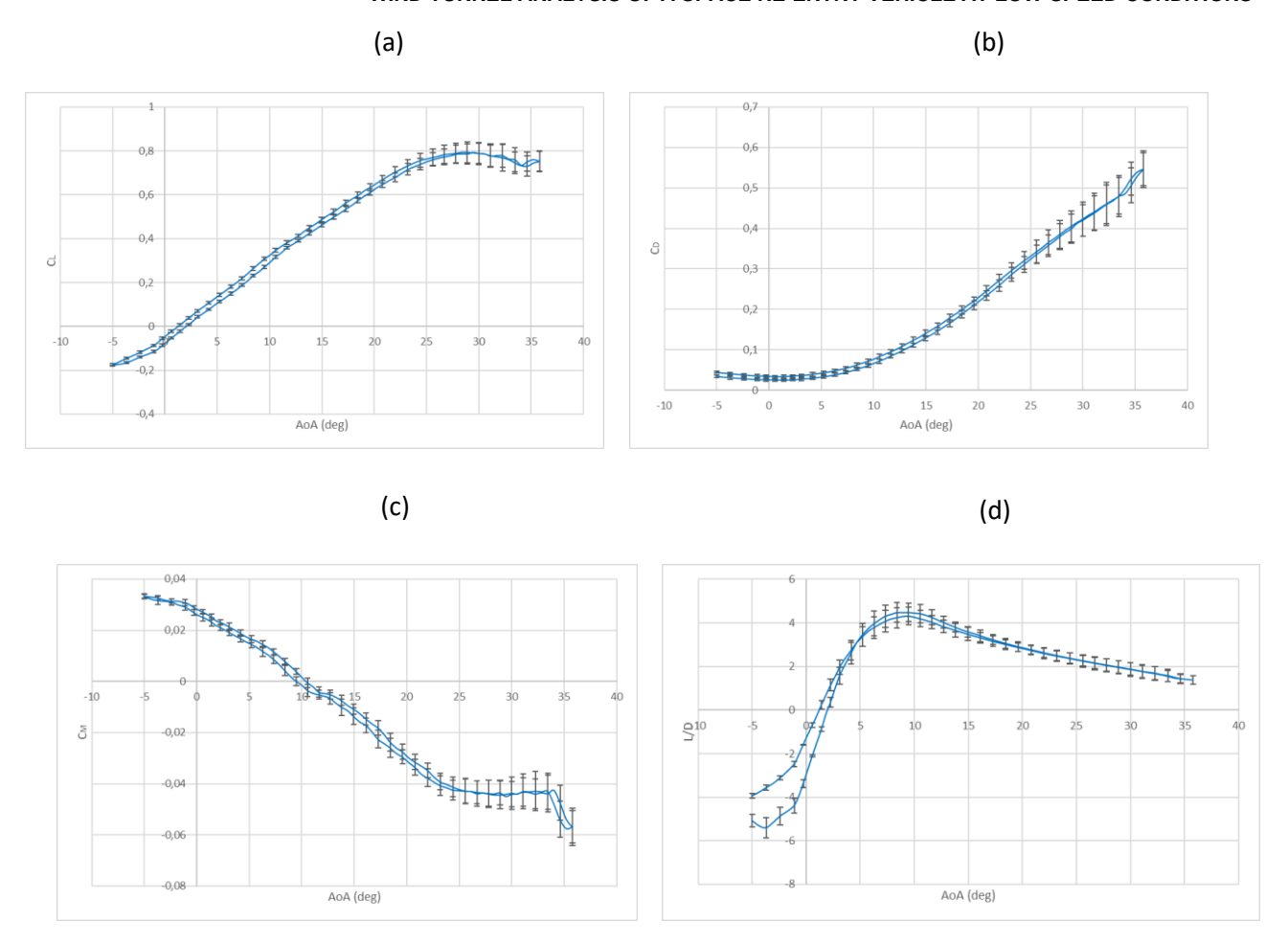


Fig. 31 - NM1 aerodynamics: (a) $C_L vs \alpha$; (b) $C_D vs \alpha$; (c) $C_M vs \alpha$ (MRP at 0.42% L_{ref}); (d) L/D $vs \alpha$.

In addition, the general trend of the data in Fig. 30a, Fig. 31a, and Fig. 32a demonstrates that the lift curve slope is highly nonlinear and varies consistently over the AoA range, according to the well-known vortex lift phenomenon [17]. In particular, for all aeroshapes, the lift stall is observed for α larger than 25 deg, as expected for a delta planform wing. At this attitude, the flowfield is dominated by unsteady separated flows due to vortex bursting [17].

In addition to the longitudinal force coefficients, Fig. 30c, Fig. 31c, and Fig. 32c provides for each aeroshape the pitching moment coefficient, C_M , about an assigned Moment Reference Center (MRC). Recall that at this stage of the spacecraft design, the vehicle CoG is still missing and so a MRC is considered for preliminary assessment of aeroshape longitudinal static stability. Therefore, the point that makes the vehicle longitudinally static stable was chosen as the pitching moment pole. Further, the chosen MRC makes the vehicle naturally trimmed at about α =10°, which is the estimated landing AoA. Considering a reference system centered in the vehicle nose, with the X-axis along the centerline toward the vehicle aft, the MRC position is 0.24 m (NM0), 0.245 m (NM1), and 0.25 m (NM2), respectively. Those MRC correspond to about 40, 41, and 43% of the vehicle length, L_{ref} , respectively. Pitching static stability is evident up to approximately 29° for aeroshapes NM0 and NM1, and 24° for aeroshape NM2, with the break in the pitching moment gradient at high angles.

For each aerodynamic coefficient provided in Fig. 30a-c, Fig. 31a-c, and Fig. 32a-c, the uncertainty bounds are also provided. As one can see, the error is minimal at low angles of attack and begin expanding from AoA≈ 25°.

Considering lift coefficient graph for each aeroshape, this point coincides with the lift curve change, as shown. In fact, at these and higher attitude conditions, the flow is highly separated and unsteady since the flow vortices start to burst, thus determining the growth in the uncertainty bounds. The L/D in Fig. 30d, Fig. 31d, and Fig. 32d shows a peak value approximately between 4.3 and 5 for the aeroshape NM0; 4.3 and 4.5 for the aeroshape NM1; 4.2 and 4.4 for the aeroshape NM2, in the [8°-12°] range.

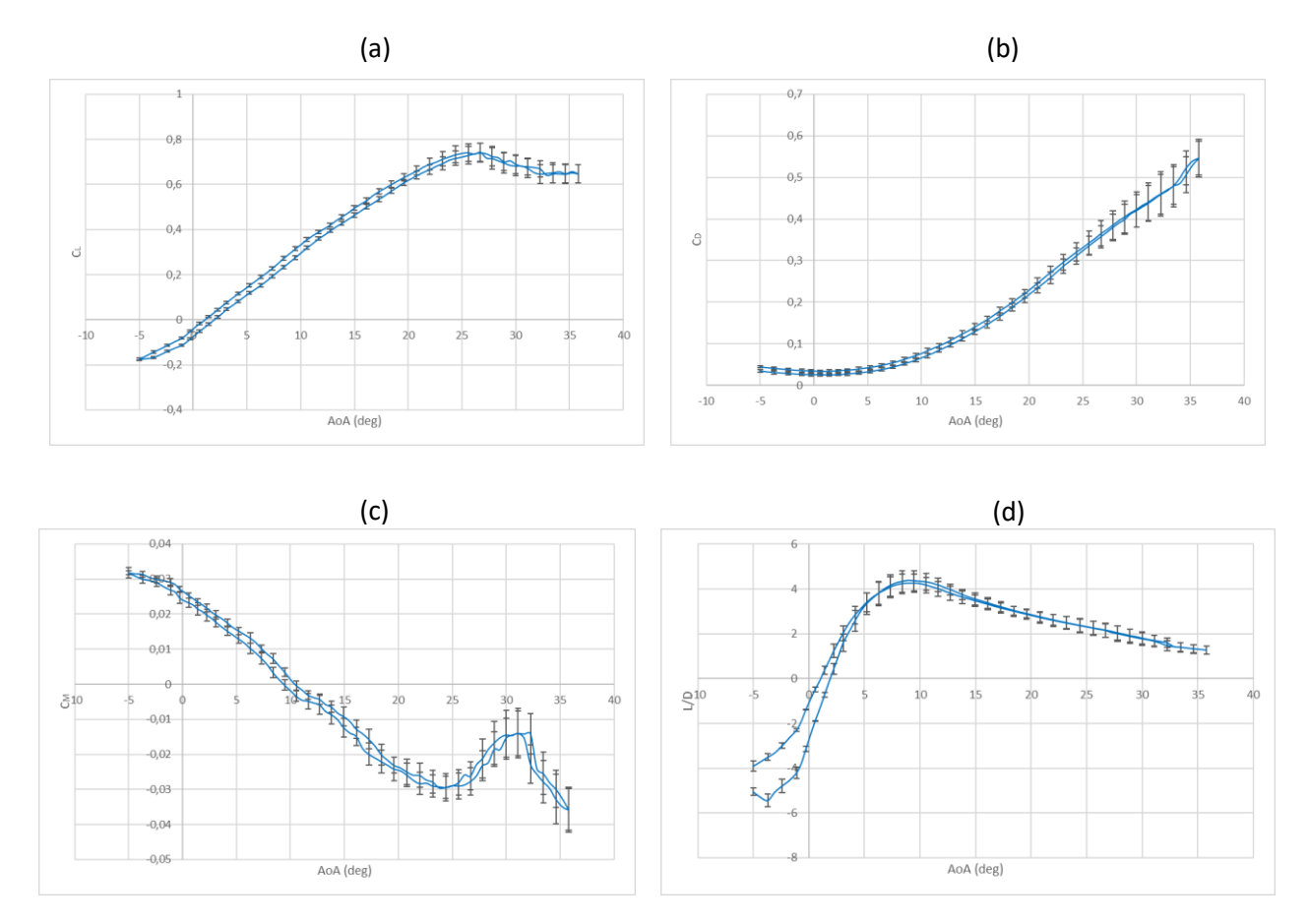


Fig. 32 - NM2 aerodynamics: (a) C_L vs α ; (b) C_D vs α ; (c) C_M vs α (MRP at 0.43% L_{ref}); (d) L/D vs α .

In Fig. 33, Fig. 34, and Fig. 35 the delta-coefficients between aeroshapes NM0 and NM1, NM0 and NM2, NM1 and NM2 are shown, respectively. As expected, aeroshapes NM0 and NM1 show a good agreement in lift and drag coefficient (see Fig. 33a-d and Table 6) because of they feature the same planform. Indeed, in both lift and drag coefficients, the maximum delta-coefficient percentage is about 2%. It is possible to notice that fluctuations in the lift and drag delta-coefficients increase starting from AoA ≈ 25° (Fig. 33b, Fig. 33d). The trend of pitching moment coefficient also seems to be similar for aeroshape NM0 and NM1 (Fig. 33e), but NM0 is more stable than NM1 in the range [10°,29°], i.e., the slope of the pitching moment curve in the range [10°,29°] of aeroshape NM0 is higher in absolute value than the NM1 one. When the pitching moment coefficient reaches the maximum value in absolute value for both aeroshapes NM0 and NM1 (AoA ≈ 29°), the delta-coefficient is about 17%, i.e., for AoA ≈ 29° the NM1 pitching moment coefficient is higher than the NM0 pitching moment coefficient by 17% (Fig. 33f). Unlike aeroshapes NMO and NM1 which exhibit very similar trends in aerodynamic coefficients, aeroshape NM2 behaves slightly differently (Table 6, Fig. 34 and Fig. 35). In particular, aeroshapes NM0 and NM1 stall gradually at AoA ≈ 29° (Fig. 30a, Fig. 31a, Fig. 33a), while aeroshape NM2 stalls rather abruptly at AoA ≈ 26° (Fig. 32a). In addition, for the aeroshapes NMO and NM1 $C_{L_{max}} \approx 0.8$ (Fig. 30a, Fig. 31a, Fig. 33a), while for NM2 $C_{L_{max}} \approx 0.7$ (Fig. 32a). In addition, drag coefficient breaks at AoA ≈ 26° (Fig. 32b), that is the point in which the aeroshape NM2 begins the stall. All these results can be explained through some second order effects that should be considered when V-tail performances are analyzed. Indeed, the reduction in lift and in the stall AoA could be the result of a flow disturbance initiated by the V-tail configuration.

At high attitude conditions, the vortex structures originated from the double-delta wing leading edges burst early due to the adverse pressure gradient promoted by the V-tail and this vortex bursting phenomenon causes reduction in L/D, as expected.

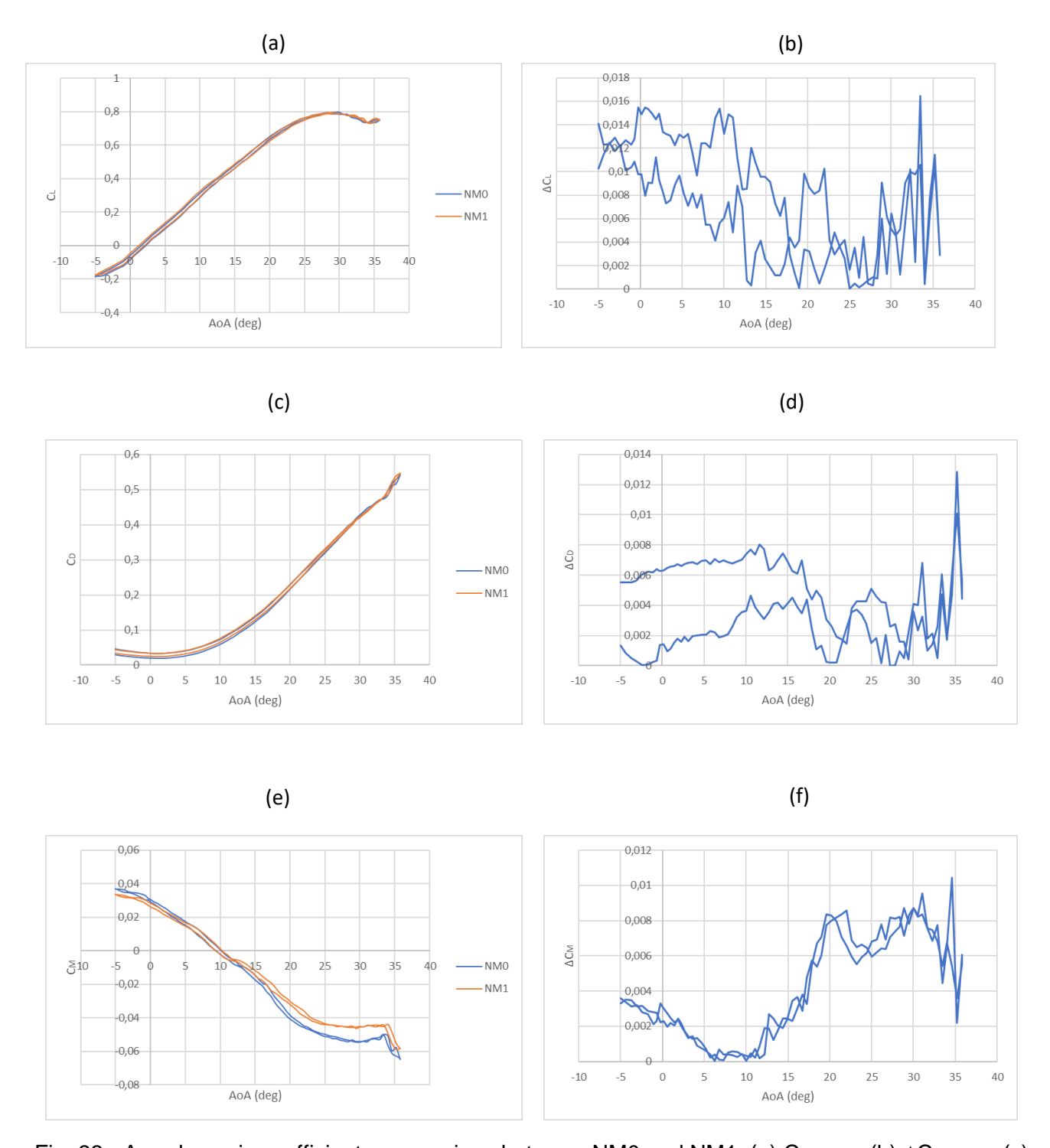


Fig. 33 - Aerodynamic coefficients comparison between NM0 and NM1: (a) C_L vs α ; (b) ΔC_L vs α ; (c) C_D vs α ; (d) ΔC_D vs α ; (e) C_M vs α ; (f) ΔC_M vs α ; (MRP at 0.41% L_{ref}).

Aeroshape NM2 presents pitching static stability in the range [10°,24°] (Fig. 32c). In that range, aeroshape NM2 presents a pitching moment coefficient curve slope lower in absolute value than aeroshapes NM0 and NM1, *i.e.*, for aeroshape NM2 $C_M \approx -0.038$ at AoA $\approx 24^\circ$, while for aeroshapes NM0 and NM1 respectively $C_M \approx -0.055$ and $C_M \approx -0.05$ at AoA $\approx 29^\circ$. Thus, for AoA between 10° and 24°, NM2 is less longitudinal stable than NM0 and NM1 (see Fig. 34e and Fig. 35e).

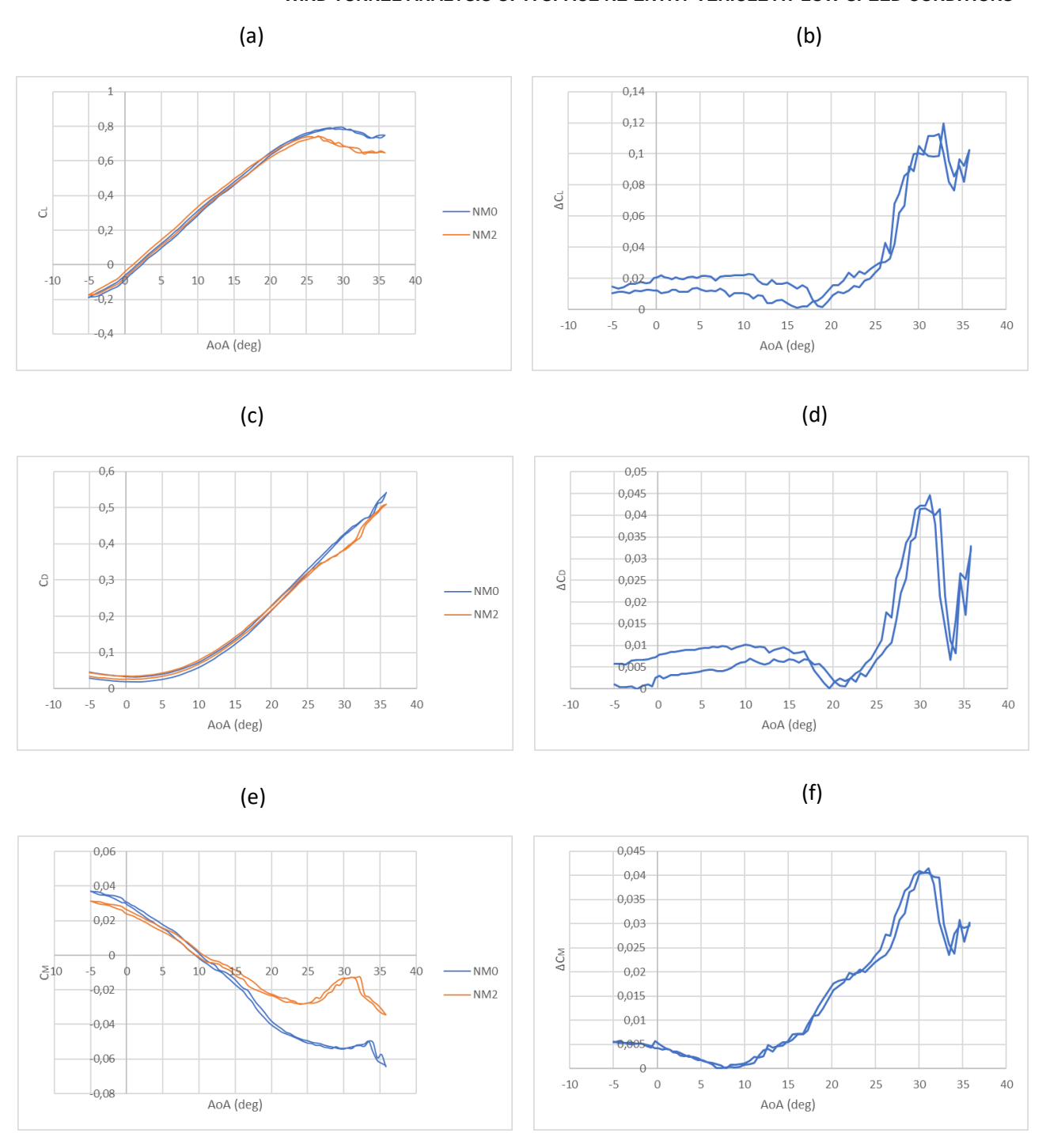


Fig. 34 - Aerodynamic coefficients comparison between NM0 and NM2: $C_L \text{ vs } \alpha$; (b) $\Delta C_L \text{ vs } \alpha$; (c) $C_D \text{ vs } \alpha$; (d) $\Delta C_D \text{ vs } \alpha$; (e) $C_M \text{ vs } \alpha$; (f) $\Delta C_M \text{ vs } \alpha$; (MRP at 0.42%L_{ref}).

All the above results seem to favor aeroshapes NM0 and NM1 for longitudinal flight conditions. However, it is important to consider that flying at high AoA can produce a turbulent or separated air wake in the area where a conventional tail would normally be mounted. A V-tail is one approach that can move the stabilizing surface up and out of this wake. Therefore, a V-tail could be favorable. Hence, analyzing aeroshapes NM3, NM4, and NM5, which all present winglets that could improve stalling conditions and longitudinal performances, is mandatory, and it is the objective of the next work. Further details about lateral and directional stability of aeroshapes NM0, NM1, and NM2, but also NM3, NM4, and NM5, will be also provided in future studies.

WIND TUNNEL ANALYSIS OF A SPACE RE-ENTRY VEHICLE AT LOW-SPEED CONDITIONS

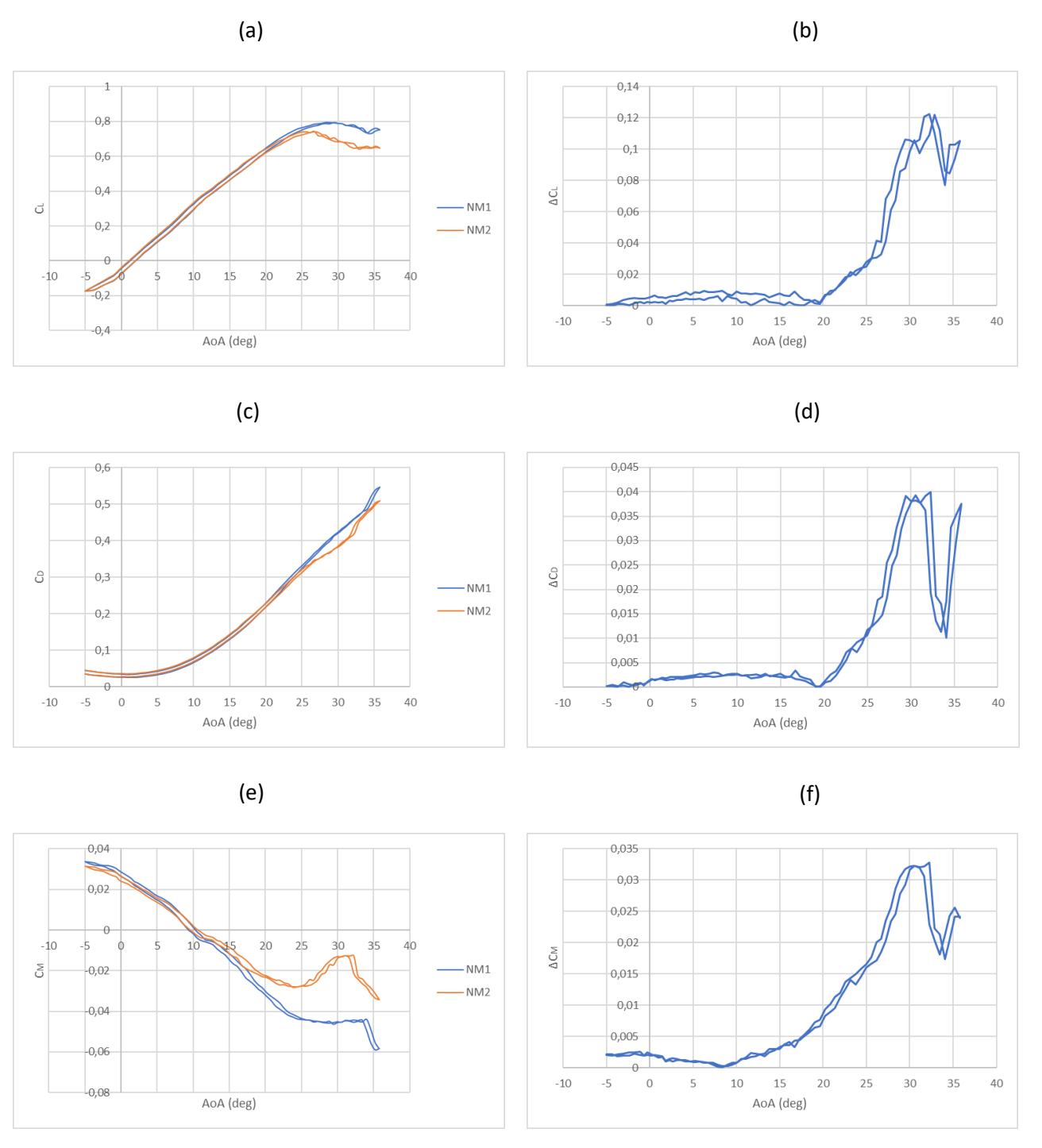


Fig. 35 - Aerodynamic coefficients comparison between NM1 and NM2: C_L vs α ; (b) ΔC_L vs α ; (c) C_D vs α ; (d) ΔC_D vs α ; (e) C_M vs α ; (f) ΔC_M vs α ; (MRP at 0.43%L_{ref}).

Table 6 – Maximum longitudinal force delta-coefficients.

Aeroshape	Δc_L	Δc_D
NM0-NM1	2%	2%
NM0-NM2	18%	11%
NM1-NM2	18%	10%

8. Conclusions

Six different crew return vehicle aeroshapes for low Earth orbit support servicing have been developed considering well-established multidisciplinary design optimization methodologies. The proprietary SBISO technique was applied to the aeroshape design to improve both longitudinal and lateral-directional stability of the vehicle. A parametric geometry model, defined using the SBISO technique, was included within a proprietary design optimization procedure to find the best aeroshape arrangement of winglets, vertical tail and/or V-tail. Low and high-speed aerodynamic performances of these configurations, as part of the optimization process, have been assessed by means of panel methods. For the assessment of the high-speed aerodynamic performances of aeroshapes, an inhouse developed tool that exploits the surface impact methods has been used. At low-speed conditions, an open-source panel method tool, based on the potential flow theory. Further, a test campaign is also carried out in wind tunnel at 30 m/s speed to verify the ability of the six aeroshapes to perform a safe landing on a conventional runway. The wind tunnel test models were built using reconfigurable assemblies of three-dimensional printed parts using several NupBox® 3D printers.

The longitudinal aerodynamic performances of aeroshapes NM0, NM1, and NM2, have been analyzed in detail and experimental results in terms of force and moment coefficients compared each other. So far, evaluated wind tunnel results show that aeroshapes NM0 and NM1 have slightly better longitudinal aerodynamics with stall conditions reached at higher attitude compared to NM2. Indeed, the V-tail of this aeroshape is expected to determine an early bursting of the flow vortices that start from the delta wing leading edges with respect to the NM0 (i.e., no tail) and NM1 (i.e., single tail) aeroshapes. Anyway, the judgment to conclude who would be the best aeroshape is postponed at the time when also the lateral-directional aerodynamic force and moment coefficients will be analyzed. In fact, there are some reasons why a V-tail design could be preferred to a conventional tail assembly. For instance, the use of a V-tail will probably be less concerned about the canopy wake, that could be significant considering that the vehicle is expected to land at a rather high angle of attack.

Finally, a V-tail should be more effective when the aeroshape will fly at high attitude during the hypersonic flight.

9. Contact author information

E-mail address: nicolina.montella@unicampania.it

Telephone number: +39 3663305513.

10. Copyright Statement

The authors confirm that they, and/or their company or organization, hold copyright on all of the original material included in this paper. The authors also confirm that they have obtained permission, from the copyright holder of any third part material included in this paper, to publish it as part of their paper. The authors confirm that they give permission, or have obtained permission from the copyright holder of this paper, for the publication and distribution of this paper as part of the ICAS proceedings or as individual off-prints from the proceedings.

References

- [1] Iuspa L., "Free topology generation of self-stiffened panels using skeleton-based integral soft objects," Computer and Structures 158, pp. 184-210, 2015.
- [2] Viviani A., Iuspa L. and Aprovitola A., "Multi-objective optimization for re-entry spacecraft conceptual design using a free-form shape generator," Aerospace Science and Technology, pp. 312-324, 2017.
- [3] Iuspa L., Aprovitola A., Pezzella G. and Viviani A., "Multidisciplinary optimization of a space re-entry vehicle using skeleton-based integral soft objects," Aerospace Scienze and Technology, vol. 131, no. 107996, 2022.
- [4] University of Sydney, "*USYD Amme Wind Tunnels*," [Online]. Available: https://sites.google.com/view/usyd-amme-wind-tunnels/home.
- [5] Viviani A., Aprovitola A., Iuspa L. and Pezzella G., "Low speed longitudinal aerodynamics of a blended wing body re-entry vehicle," Aerospace Science and Technology, vol. 107, no. 106303, 2020.

WIND TUNNEL ANALYSIS OF A SPACE RE-ENTRY VEHICLE AT LOW-SPEED CONDITIONS

- [6] Montella N., Aprovitola A., Iuspa L. and Pezzella G., "Aeroshape and Trajectory Design of Next Generation Reentry Vehicles," in 33rd Congress of the International Council of the Aeronautical Sciences (ICAS-2022) September 4-9, 2022., Stockholm, Sweden, 2022.
- [7] University of Sydney, "*AMME Lab Wiki*," [Online]. Available: https://wiki.ammelabs.org/fablab/training/process/start.
- [8] Viviani A., Aprovitola A., Iuspa A. and Pezzella G., "Aerospace design of reusable re-entry vehicles by multidisciplinary optimization and computational fluid dynamics," Aerospac Science and Technology, vol. 105, no. 106029, 2020.
- [9] "Apame 3d panel method," [Online]. Available: http://www.3dpanelmethod.com.
- [10] Bertin J., Hypersonic Aerothermodynamics, The American Institute of Aeronautics and Astronautics (AIAA), 1994.
- [11] Gentry A. E., Smyth D. N. and Oliver W. R., *The Mark IV supersonic-hypersonic arbitrary-body program. Volume II. Program formulation*, National Technical Information Service, 1973.
- [12] Aprovitola A., Montella N., Iuspa L., Pezzella G. and Viviani A., "An optimal heat-flux targeting procedure for leo re-entry of reusable vehicles," Aerospace Science and Technology, vol. 112, no. 106608, 2021.
- [13] Barlow J., Rae W. and Pope A., Low-speed wind tunnel testing, NY, USA: John Wiley & Sons Inc.: New York, 1999, p. 728.
- [14] Anderson M. J., A Methodology for Aerodynamic Parameter Estimation of Tail-Sitting Multi-Rotors Ph.D. Thesis, Sydney, Australia: The University of Sydney, 2017.
- [15] Lehmkuehler K., A Direct Comparison of Small Aircraft Dynamics between Wind Tunnel and Flight Tests. Ph.D. Thesis, Sydney, Australia: The University of Sydney, 2016.
- [16] Giannelis N. F., Bykerk T. and a. Vio G. A., "A Generic Model for Benchmark Aerodynamic Analysis of Fifth-Generation High-Performance Aircraft," Aerospace, vol. 10, no. 9, p. 746, 2023.
- [17] Giannino S. M., Pezzella G. and Viviani A., "Low Speed Aerodynamics of Six Optimised and Unconventional Re-Entry Vehicle Aeroshapes," in 34th Congress of the International Council of the Aeronautical Sciences. ICAS2024_0864, Florence, 2024.
- [18] Purser P. E. and Campbell J. P., "Experimental Verification of a Simplified Vee-Tail Theory and Analysis of Available Data on Complete Models with Vee-Tails," National Advisory Committee for Aeronautics, Langley Field, 1944.